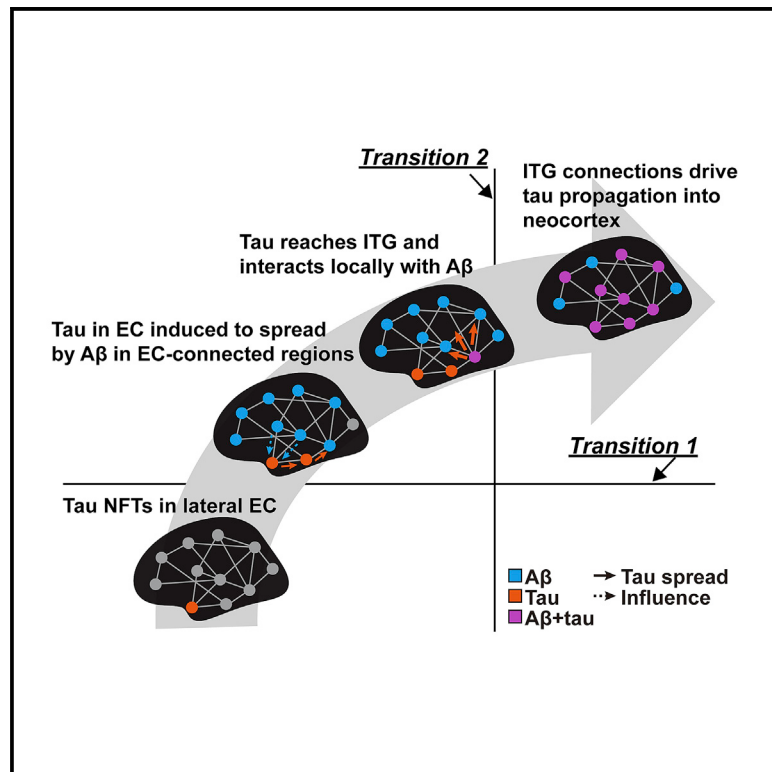


Regional A β -tau interactions promote onset and acceleration of Alzheimer's disease tau spreading

Graphical abstract



Authors

Wha Jin Lee, Jesse A. Brown,
Hye Ryun Kim, ..., Joon-Kyung Seong,
William W. Seeley, Alzheimer's
Disease Neuroimaging Initiative

Correspondence

jkseong@korea.ac.kr (J.-K.S.),
bill.seeley@ucsf.edu (W.W.S.)

In brief

Lee et al. show that the natural history of AD traverses a critical period that begins once A β emerges within entorhinal cortex (EC)-connected regions, continues as tau spreads from the EC into connected mesial temporal and limbic regions, and may end once A β and tau interact within the inferior temporal gyrus propagation hubs, whose connections are well suited to facilitate widespread neocortical tau propagation.

Highlights

- Network flow-based model identifies tau propagation hubs in inferior temporal gyri
- Remote A β -tau interactions in entorhinal cortex may trigger initial tau spreading
- Local A β -tau interactions in inferior temporal gyrus may promote tau propagation
- Connectivity-based model addresses the spatial incongruity between early A β and tau



Article

Regional A β -tau interactions promote onset and acceleration of Alzheimer's disease tau spreading

Wha Jin Lee,¹ Jesse A. Brown,^{2,3} Hye Ryun Kim,^{1,4} Renaud La Joie,^{2,3} Hanna Cho,⁵ Chul Hyoung Lyoo,⁵ Gil D. Rabinovici,^{2,3,6} Joon-Kyung Seong,^{1,7,10,*} William W. Seeley,^{2,3,8,10,11,*} and Alzheimer's Disease Neuroimaging Initiative⁹

¹School of Biomedical Engineering, Korea University, Seoul 02841, South Korea

²Department of Neurology, Memory and Aging Center, University of California, San Francisco, San Francisco, CA 94143, USA

³Weill Institute for Neurosciences, University of California, San Francisco, San Francisco, CA 94143, USA

⁴Global Health Technology Research Center, College of Health Science, Korea University, Seoul 02841, South Korea

⁵Department of Neurology, Gangnam Severance Hospital, Seoul 06273, South Korea

⁶Department of Radiology and Biomedical Imaging, University of California, San Francisco, San Francisco, CA 94143, USA

⁷Department of Artificial Intelligence, Korea University, Seoul 02841, South Korea

⁸Department of Pathology, University of California, San Francisco, San Francisco, CA 94143, USA

⁹Data used in preparation of this article were obtained from the Alzheimer's Disease Neuroimaging Initiative (ADNI) database (adni.loni.usc.edu). As such, the investigators within the ADNI contributed to the design and implementation of ADNI and/or provided data but did not participate in analysis or writing of this report. A complete listing of ADNI investigators can be found at: http://adni.loni.usc.edu/wp-content/uploads/how_to_apply/ADNI_Acknowledgement_List.pdf

¹⁰These authors contributed equally

¹¹Lead contact

*Correspondence: jkseong@korea.ac.kr (J.-K.S.), bill.seeley@ucsf.edu (W.W.S.)

<https://doi.org/10.1016/j.neuron.2022.03.034>

SUMMARY

Amyloid-beta and tau are key molecules in the pathogenesis of Alzheimer's disease, but it remains unclear how these proteins interact to promote disease. Here, by combining cross-sectional and longitudinal molecular imaging and network connectivity analyses in living humans, we identified two amyloid-beta/tau interactions associated with the onset and propagation of tau spreading. First, we show that the lateral entorhinal cortex, an early site of tau neurofibrillary tangle formation, is subject to remote, connectivity-mediated amyloid-beta/tau interactions linked to initial tau spreading. Second, we identify the inferior temporal gyrus as the region featuring the greatest local amyloid-beta/tau interactions and a connectivity profile well suited to accelerate tau propagation. Taken together, our data address long-standing questions regarding the topographical dissimilarity between early amyloid-beta and tau deposition.

INTRODUCTION

Brain parenchymal amyloid-beta (A β) deposition and tau neurofibrillary tangle formation are the defining pathological features of Alzheimer's disease (AD) (Braak et al., 2006; Jagust, 2018; Musiek and Holtzman, 2012). A β has been proposed to trigger tau spreading (Musiek and Holtzman, 2012; Jagust, 2018), but the spatial incongruity of A β and tau during early AD has cast doubt on this hypothesis (Jagust, 2018). Whereas A β deposition begins in heteromodal association neocortices (Thal et al., 2002), the earliest forebrain neurofibrillary tangles are seen within the lateral entorhinal cortex (EC) (Hyman et al., 1984). From there, tau spreads into other mesial temporal memory structures but rarely beyond the basal temporal cortex in the absence of widespread neocortical A β deposition (Crary et al., 2014; Johnson et al., 2016; Sanchez et al., 2021a). Considering these observations, how can remote neocortical A β influence early

pathological tau, triggering it to leave the EC? How, in turn, does A β facilitate widespread tau propagation throughout the neocortex?

Recent *in vivo* evidence supports the view that tau pathophysiology exhibits a nonlinear acceleration during the natural history of AD (McDade et al., 2018; Jack et al., 2010), and understanding the basis for this acceleration represents an important priority for AD research. Human post-mortem (Braak and Del Tredici, 2011; Kim et al., 2020), *in vivo* brain imaging (Zhou et al., 2012; Raj et al., 2015; Brown et al., 2019; Vogel et al., 2020; Ossenkoppele et al., 2019; Franzmeier et al., 2020), and model-based (Liu et al., 2012; Clavaguera et al., 2013) studies have converged to suggest that transneuronal tau spreading likely contributes to the progressive large-scale network degeneration seen in AD and other tau-based disorders. We, and others, have used the normative functional and structural connectome to predict the spatial patterning and spread of atrophy (Zhou et al., 2012; Raj



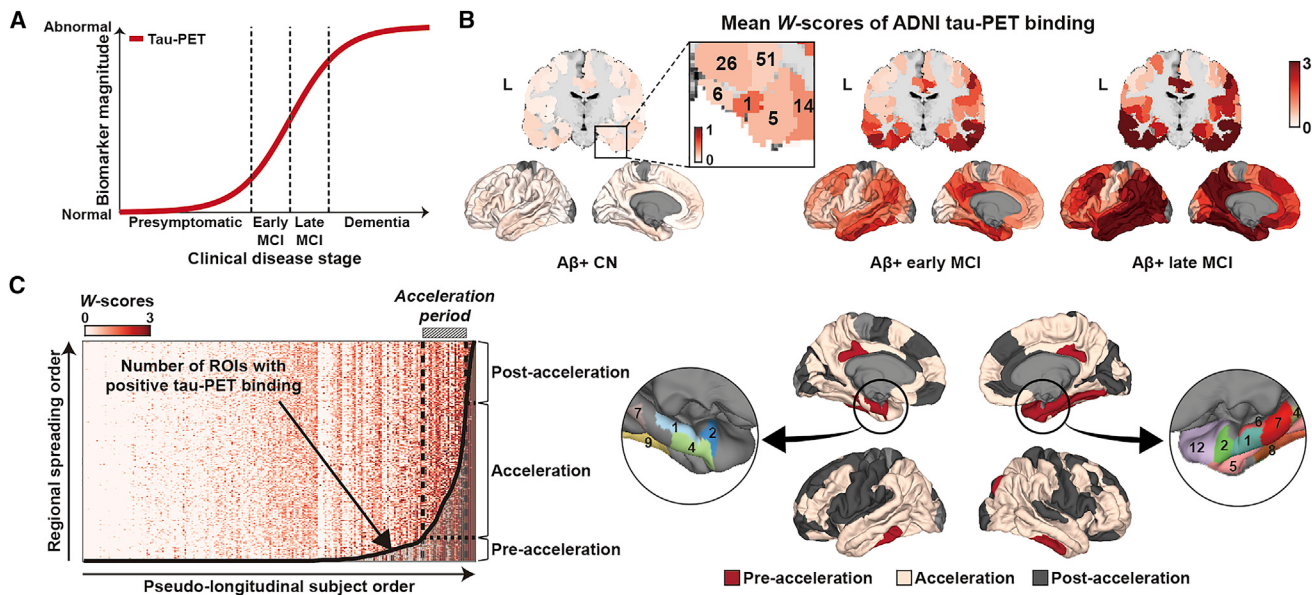


Figure 1. Pseudo-longitudinal tau regional spreading order

(A) Dynamic biomarker models of AD (Jack et al., 2010; Leuzy et al., 2019) propose that tau aggregation undergoes nonlinear acceleration in early MCI.

(B) Tau-PET data from the ADNI cohort (present study) support this concept by demonstrating a sharp increase in brain-wide tau deposition that begins in A β + subjects with early MCI and accelerates in late MCI. Color bar in A β + CN inset indicates tau-PET W-scores.

(C) Across the presymptomatic and prodromal AD cohorts, we estimated the sequence of regional tau-PET positivity in a data-driven, pseudo-longitudinal manner, using the group-level frequency distribution to infer the order. Subjects were sorted based on the number of tau-PET-positive ROIs, and tau-PET-positive regions in subjects representing the pre-acceleration, acceleration, and post-acceleration periods are shown. The acceleration period was defined as beginning where the slope in the frequency graph becomes greater than two and ending where that slope shows a second inflection, such that the second derivative becomes zero. Number labels on magnified insets (B and C) show ranks, within each hemisphere, from the frequency distribution of tau-PET positivity. This approach identifies the entorhinal cortex (region labeled 1 in insets) as the most frequently tau-positive region, in keeping with cross-sectional neuropathological data (Braak and Braak, 1991). AD, Alzheimer's disease; PET, positron emission tomography; MCI, mild cognitive impairment; CN, cognitively normal; ROI, region of interest.

et al., 2012, 2015), and early tau-positron emission tomography (PET) studies suggest connectivity-related tau patterning in AD (Ossenkoppele et al., 2019; Vogel et al., 2020; Sepulcre et al., 2018). To date, however, no study has provided a connectivity-based molecular-anatomical framework for understanding the onset and acceleration of tau spreading in AD.

In this study, we combined *in vivo* molecular imaging and large-scale brain network mapping techniques to address the long-standing questions of how regional A β and tau interact to promote the onset and acceleration of tau spreading in individuals with presymptomatic and prodromal AD. Our findings suggest that (1) remote A β incites tau spreading by interacting, via long-range connections, with tau in the EC whereas (2) local A β -tau interactions in the inferior temporal gyrus (ITG) facilitate widespread, connectivity-based tau propagation into neocortical regions that become tau-positive during the tau acceleration phase.

RESULTS

Early entorhinal tauopathy and exponential tau acceleration during prodromal AD

To capture the nonlinear acceleration of AD tau spreading (Figure 1A), we studied individuals enrolled in a multicenter observational study, the AD Neuroimaging Initiative (ADNI),

who underwent cross-sectional ^{18}F -florbetapir-PET (henceforth “amyloid-PET”) and ^{18}F -flortaucipir-PET (henceforth “tau-PET”) imaging (see Table 1). First, we mapped regions of tau-PET positivity in presymptomatic (A β +, cognitively normal [CN], n = 67) and prodromal AD (A β +, early [n = 28] and late [n = 17] mild cognitive impairment [MCI]; see STAR Methods). Tau-PET positivity in presymptomatic AD was mild, but the EC (A28/34, A35/36r) stood out as a region with high mean tau-PET signal (Figure 1B). This tau-PET mapping approach also revealed the expected sharp increase in brain-wide tau deposition in patients with late MCI. Second, we calculated the number of tau-positive brain regions for each subject within these groups (see STAR Methods). Based on the resulting frequency distribution for regional tau burden, we constructed a pseudo-longitudinal disease severity order, with the least severe subjects being those with the fewest tau-PET-positive regions. This approach identified the EC (A28/34, A35/36r) as the earliest region to become tau-positive, based on the frequency distribution within each hemisphere. Overall, these approaches, which use cross-sectional data to make longitudinal inferences, converged to broadly reproduce the canonical stages of tau neurofibrillary tangle formation inferred from human neuropathological studies (Braak and Braak, 1991) (see Table S1). Most importantly, this dataset enabled us to identify an apparent “acceleration phase” of exponential spreading in the spatial extent of tau-PET

Table 1. Demographic and clinical characteristics of the overall study population

ADNI discovery dataset	CN (n = 182)	Early MCI (n = 62)	Late MCI (n = 30)	AD dementia (n = 9)	Group comparison p value (statistics)
Age (years)	75.29 ± 7.77	75.79 ± 6.82	74.77 ± 7.56	69.56 ± 10.0	0.309
Sex (female, n [%])	105 (57.7)	24 (38.7)	13 (43.3)	3 (33.3)	0.032 (8.835)
Education (years)	16.63 ± 2.52	16.40 ± 2.74	16.67 ± 2.68	15.44 ± 2.24	0.496
MMSE	28.96 ± 1.32	27.43 ± 3.13	25.63 ± 5.56	21.44 ± 1.67	<0.001
CDR SOB	0.16 ± 0.52	1.98 ± 2.47	2.97 ± 3.56	3.83 ± 1.62	<0.001
Amyloid positivity (%) [*]	67 (36.8)	28 (45.2)	17 (56.7)	9 (100.0)	<0.001 (17.194)
Korean validation dataset	CN (n = 96)	aMCI (n = 84)	AD dementia (n = 71)	Group comparison p value (statistics)	
Age (years)	66.31 ± 9.49	71.32 ± 9.12	74.37 ± 9.35	<0.001	
Sex (female, n [%])	60 (66.7)	51 (60.7)	54 (76.1)	0.093 (4.744)	
Education (years)	11.94 ± 4.54	11.46 ± 4.26	9.77 ± 5.72	0.047	
MMSE	28.19 ± 1.78	25.63 ± 2.80	19.08 ± 5.33	<0.001	
CDR SOB	0.00 ± 0.00	1.61 ± 1.01	5.01 ± 2.54	<0.001	
Amyloid positivity (%) [*]	9 (9.4)	45 (53.6)	56 (78.9)	<0.001 (84.947)	
Longitudinal dataset	CN (n = 146)	MCI (n = 114)	AD dementia (n = 44)	Group comparison p value (statistics)	
N (ADNI/Korean)	72/74	55/59	8/36	<0.001 (14.363)	
Follow-up (years)	1.84 ± 0.53	1.69 ± 0.49	1.86 ± 0.41	0.016	
Age (years)	71.25 ± 9.70	72.82 ± 7.49	73.50 ± 9.34	0.143	
Sex (female, n [%])	88 (60.3)	59 (51.8)	30 (68.2)	0.135 (4.008)	
Education (years)	14.22 ± 4.16	13.73 ± 4.46	10.27 ± 5.74	<0.001	
MMSE	28.59 ± 1.60	26.46 ± 3.27	20.52 ± 4.15	<0.001	
CDR SOB	0.12 ± 0.46	1.38 ± 1.31	4.39 ± 1.64	<0.001	
Amyloid positivity (%) [*]	40 (27.4)	68 (59.6)	36 (81.8)	<0.001 (51.199)	

Data are presented as mean ± standard deviation for continuous variables and number (%) for nominal variables. Independent Kruskal-Wallis test for continuous variables and chi square test for nominal variables.

CN, cognitively normal; early MCI, early mild cognitive impairment; late MCI, late mild cognitive impairment; AD, Alzheimer's disease; MMSE, mini-mental state examination; CDR SOB, clinical dementia rating sum-of-boxes; aMCI, amnestic mild cognitive impairment.

*Note that only amyloid-PET-positive subjects were included in subsequent analyses.

positivity and, in turn, the regions that exhibit tau-PET positivity before, during, and after this tau acceleration phase (**Figure 1C**). The tau regional spreading order was generally robust across a range of tau W-score thresholds (**Figure S1**), and the key findings shown in **Figure 1** were replicated in an independent sample of older subjects from across the AD clinical spectrum (henceforth, "Korean validation dataset," see **STAR Methods** and **Figures S1** and **S2**). Importantly, the Korean validation dataset included a larger proportion of subjects with more advanced clinical AD (see **Table 1**), suggesting that the identified acceleration phase did not result simply from analyzing an ADNI sample skewed toward early AD stages.

A network flow-based model identifies the inferior temporal gyri as key tau propagation hubs

To clarify the anatomical basis for accelerated tau spreading, we used diffusion tensor imaging to construct a normative "connectome," a matrix describing the group-level structural connectivity between each pair of brain regions. We then used this connectome to create a network flow-based model for simulating tau propagation along region-to-region macro-scale

connections (**Figure 2A**). This model enabled us to identify brain regions well positioned to promote widespread tau aggregation (henceforth, "propagation hubs") and to clarify how Aβ deposition relates to initial and accelerated tau spreading. Applying the principles of graph theory, we modeled connectivity-mediated tau spreading based on maximum inter-nodal flow, which considers multiple distinct paths between any two nodes (**Figure 2A**). We then searched a pool of 213 regions, after removing regions prone to off-target tau-PET binding (i.e., radiotracer binding to non-tau targets; see **Table S2**), with the goal of identifying tau propagation hubs. Specifically, we searched a library of normative network flow-based connectivity maps, each based on a single candidate brain region or "seed" (**Figure 2B**), seeking to identify regions whose connectivity most resembles the regions into which tau spreads during the tau acceleration phase. To this end, we estimated the goodness-of-fit (GOF) between each seed's map and the topography of the tau acceleration phase, representing the tau acceleration phase by generating seven pairs of binary inner and outer masks across a range of spatial extents. Masks were gradually expanded to mimic tau propagation (**Figure S3**) and to avoid potential influences of

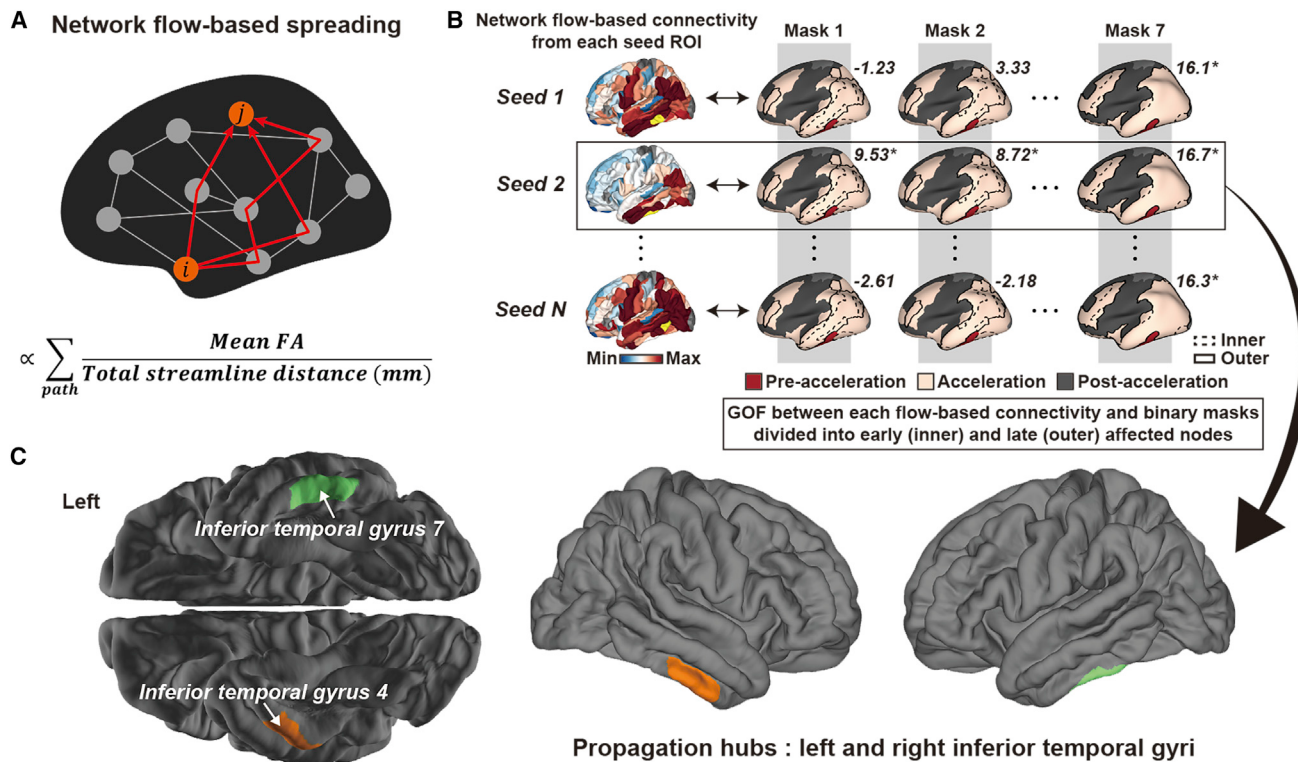


Figure 2. A network flow-based tau spreading model identifies tau propagation hubs in the inferior temporal gyrus

(A) A simplified network graph illustrates the network flow-based propagation model of tau spreading. Circles represent brain regions (nodes), and lines represent structural connections between node pairs (edges). The network flow-based model adopts a definition of maximum inter-nodal flow, which considers multiple distinct paths. Tau spreading from node i to node j is proportional to the total flow value, which is calculated as the sum of the maximum flow for each possible path.

(B) Searching across all brain regions (examples in yellow shading), propagation hubs were identified based on the goodness-of-fit (GOF) of their network flow-based connectivity maps, derived from healthy controls, to 7 pairs of binary inner/outer masks defined using the regions that represent the tau acceleration phase (see [Figure 1C](#) and [STAR Methods](#); GOF scores from example seed ROIs are shown).

(C) Two regions were identified as propagation hubs, having significant GOF scores across all inner/outer mask thresholds, and both were subregions of the inferior temporal gyrus (ITG). FA, fractional anisotropy; ROI, region of interest.

arbitrary thresholding and mask definition. Finally, we identified propagation hubs, using a stringent set of criteria, as those nodes with significant GOF scores (permutation-based one-sample t test, Bonferroni corrected $p < 0.05$) across all seven inner/outer mask pairs (see [STAR Methods](#)). Based on this brain-wide search strategy, the left and right ITG emerged, independently, as propagation hubs ([Figure 2C](#)), and this finding was stable after varying the total number of inner/outer mask pairs used to represent the acceleration phase ([Table S3](#)).

As expected, the network flow-based connectivity maps seeded by these ITG propagation hubs were strongly correlated with the topography of tau deposition seen in subjects representing the tau acceleration phase (contrasted with pre-acceleration phase subjects; [Figures 3A and 3B](#); see [STAR Methods](#)), and those correlations were stronger than seen for other brain regions (based on null hypothesis distributions; [Figure 3C](#)) ([Scott et al., 2020](#)). Compared with other network-based propagation models developed through our previous work ([Brown et al., 2019](#); [Zhou et al., 2012](#)), the network flow-based model produced the highest correlations between the ITG propagation hub connectivity pattern and the acceleration phase tau

deposition topography (see [Figure S4](#)), justifying our use of the network flow-based model for propagation hub identification. Applying the same propagation hub identification procedure to the Korean validation dataset, we again identified the two ADNI-derived ITG areas, and the connectivity of these regions correlated strongly with the pattern of acceleration phase tau deposition topography ([Figure S4B](#)). We also identified three additional putative propagation hubs, all within the ITG regions bilaterally (see [Figure S5](#)). Because tau-PET image analysis methods continue to evolve, we also reproduced these key findings after varying several methodological steps that remain unsettled in the field (see [Tables S4](#) and [S5](#)).

Remote and local A β -tau interactions are associated with initial and accelerated tau spreading

AD has been conceptualized as an A β -triggered tauopathy ([Musiek and Holtzman, 2012](#)), but to date it has been difficult to reconcile this concept with the topographical discordance between early A β and tau deposition in humans. Having (1) confirmed the EC as the forebrain region from which initial tau spreading occurs and (2) identified the bilateral ITG regions as

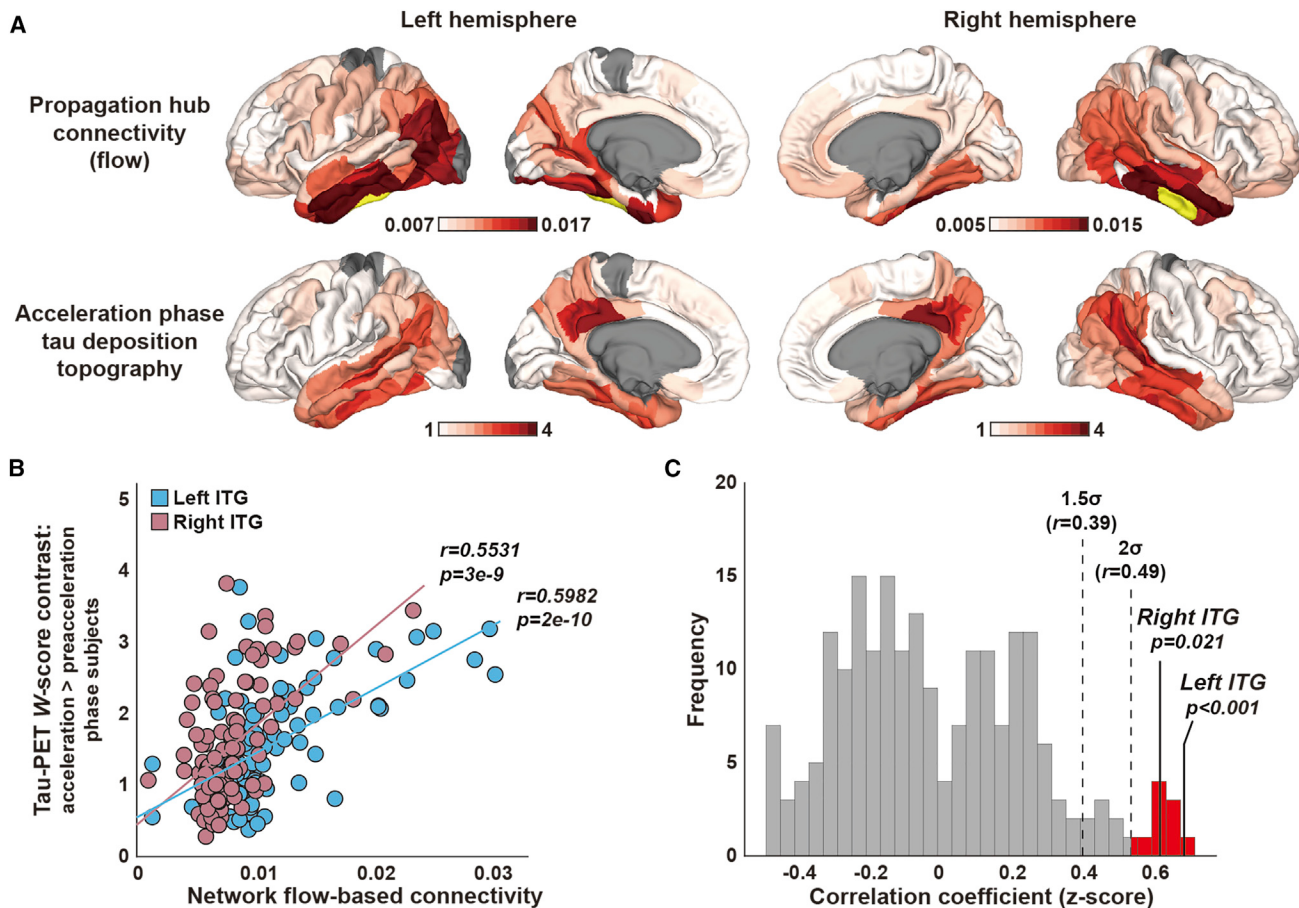


Figure 3. Inferior temporal gyrus connectivity mirrors tau acceleration phase topography

(A) Using the network flow-based model, we examined the connectivity patterns of the two inferior temporal gyrus regions (highlighted in yellow) identified as propagation hubs. The connectivity maps of these hubs resembled the acceleration phase tau deposition topography, derived by averaging *W*-score contrasts across all 1,560 subject pairs representing the acceleration and pre-acceleration phases.

(B) The connectivity values and the acceleration phase tau deposition topography map show high spatial correlation for both hemispheres.

(C) Null hypothesis distributions are shown for spatial correlations between the total network flow-based maps and acceleration phase tau deposition topography. The correlation coefficients were converted to Z-scores, and the corresponding one-tailed *p* values were obtained for the two ITG propagation hubs. The red areas show correlation coefficients more than 2 SD greater than the mean. PET, positron emission tomography; ITG, inferior temporal gyrus; SD, standard deviation.

tau propagation hubs, we sought to determine whether and how A β might interact with tau in the EC and ITG to induce and accelerate tau spreading. To this end, we developed a network-based model to estimate two types of A β -tau interaction: remote and local (Figure 4A). Remote interactions were conceived as arising from each tau-positive region's connectivity to A β -positive regions. More specifically, we imagined that tau-positive regions contain tau-positive neurons, whose axons travel to and form synapses with neurons residing in A β -positive regions. Specific A β species may, in turn, prove toxic to those synapses or may otherwise influence axons arriving from or departing to remotely connected, tau-positive neurons, thereby triggering a long-range interaction with the tau-positive region. Local interaction, by contrast, was conceived as the direct co-mingling of parenchymal A β and aggregating tau within a given brain region (He et al., 2018).

Calculation of remote A β -tau interactions required three steps. First, we calculated each region of interest's weighted

connectivity strength, derived from the healthy structural connectome, to all other regions. Second, we multiplied each connectivity strength by the magnitude of A β -deposition within the connected region and summed these products to calculate a connectivity-weighted remote A β influence metric. Finally, the remote A β influence metric was multiplied by the magnitude of tau deposition within the region of interest (Figure 4A). To rank regions according to their remote A β -tau interactions, we again applied the frequency distribution method, assuming that regions with the earliest remote A β -tau interactions would be those in which these connectivity-mediated interactions were detected in the largest proportion of patients (see STAR Methods). Using this approach, we found that the lateral EC (A35/36r) ranked first among 213 brain regions (Figures 4B and S7). Based on absolute levels, the lateral EC showed significantly greater remote A β -tau interaction than the median of all other brain regions (t : 3.63/2.61, FDR-corrected *p* value: 0.001/0.017, left/right EC). This finding

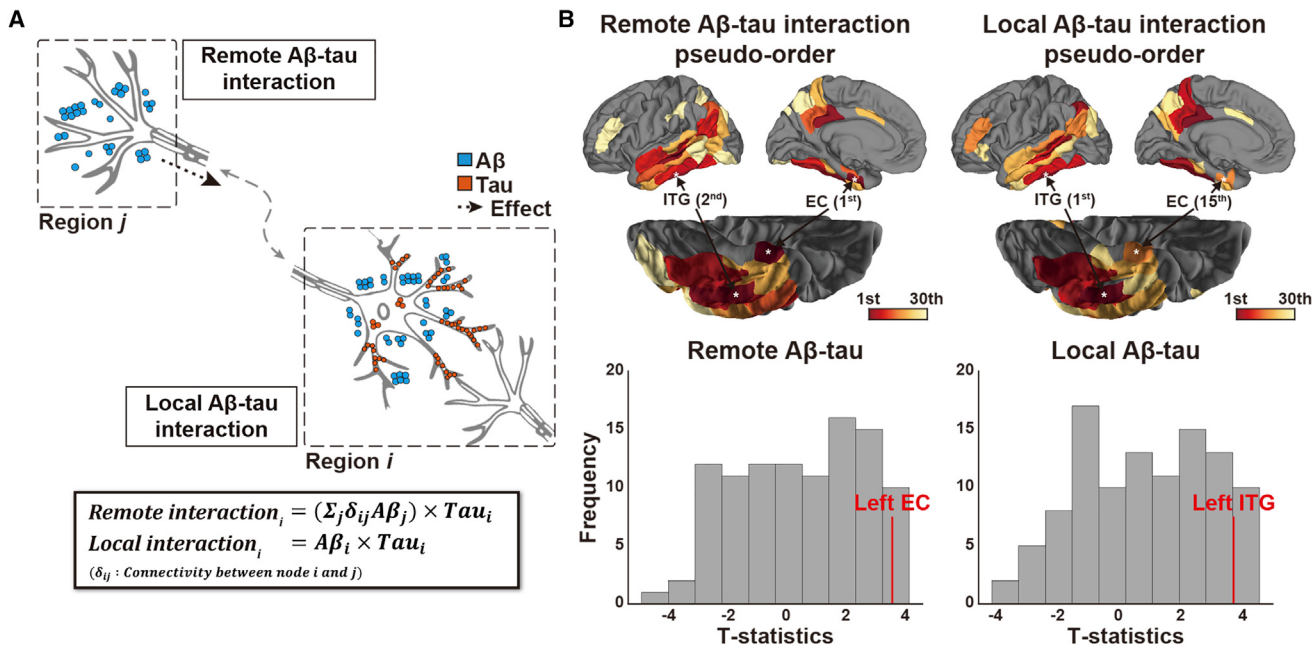


Figure 4. Network-based Aβ-tau interaction model

(A) Aβ-tau interactions were modeled using two interaction types: remote and local. Remote interaction measures the effect of Aβ deposition within regions to which a given region is connected, weighted by the strength of those connections, whereas local interaction requires the presence of Aβ and tau deposition within the same region.

(B) For remote Aβ-tau interactions, the lateral EC regions ranked first within the frequency distribution for each hemisphere. By contrast, the identified left and right ITG propagation hubs ranked first and second for local Aβ-tau interaction frequency within left and right hemisphere, respectively. T-statistic distributions of continuous remote Aβ-tau and local Aβ-tau interaction values also show greater interactions in the lateral EC and ITG, respectively, compared with other brain regions. ITG, inferior temporal gyrus.

was stable across a range of tau *W*-score thresholds (Figure S6) and alternative tau-PET analysis methods (Tables S4 and S5) and was broadly replicated in the Korean validation dataset, in which the lateral EC had the highest median remote Aβ-tau interaction rank of any brain region (EC left: 4th, EC right: 1st; Figures S6 and S7). Robustness of this finding across a range of *W*-score thresholds was even more evident in the Korean validation dataset, perhaps because this dataset represents a more homogeneous cohort evaluated at a single center.

To calculate local Aβ-tau interactions, we multiplied each region's local Aβ deposition (amyloid-PET standardized uptake value ratio [SUVR] value) by its tau-PET *W*-score. Although the procedures for calculating local Aβ-tau interactions and those for identifying propagation hubs were completely independent, the left and right ITG propagation hubs emerged as the highest-ranking regions, brain-wide, for local Aβ-tau interaction (Figures 4B and S7). Local Aβ-tau interaction scores for the left and right ITG were significantly greater than the median of all other regions (*t*: 3.77/4.28, FDR-corrected *p* value: <0.001/<0.001, left/right ITG). This finding was stable across a range of tau *W*-score thresholds (Figure S6) and alternative tau-PET analysis methods (Tables S4 and S5). These findings were also broadly reproduced in the Korean validation dataset (Figures S6 and S7), in which the ITG hubs for each hemisphere ranked in the top 4 for local Aβ-tau interaction within that hemisphere (ITG7, right: 4th; ITG4, left: 3rd), with the few higher-ranking regions being adjacent basal temporal areas.

Longitudinal tau aggregation trajectories support the Aβ-tau interaction model

In the preceding analyses, we used cross-sectional data to make longitudinal inferences about the natural history of AD. This strategy enabled us to derive a regional tau spreading order based on a sufficient sample size; nonetheless, the pseudo-longitudinal approach cannot directly test the within-subjects temporal predictions made by our model. To address this limitation, we collected all subjects in the ADNI (*n* = 135) and Korean (*n* = 169) cohorts who had undergone at least one follow-up structural MRI and tau-PET scan (see Table 1). Since the two longitudinal samples were relatively small, we combined them into a single ADNI/Korean longitudinal MCI cohort after regularizing the two datasets separately using the *W*-score approach (see STAR Methods). Using this combined cohort, we first determined the regional tau accumulation rate, defined as the annualized change in the tau-PET *W*-score. As expected, tau accumulation in subjects with Aβ+ MCI (*n* = 68) is most prominent in basal temporal areas and, to a lesser extent, in fronto-parietal heteromodal association cortices (Figure 5A). Next, we returned to our library of normative network flow-based maps, one derived from each brain region, to determine the spatial correlation between each region's connectivity pattern and the longitudinal tau accumulation seen in Aβ+ MCI. Remarkably, mirroring the cross-sectional findings, the ITG regions again stood out as the regions whose connectivity best matched the longitudinal tau accumulation pattern (Figure 5A).

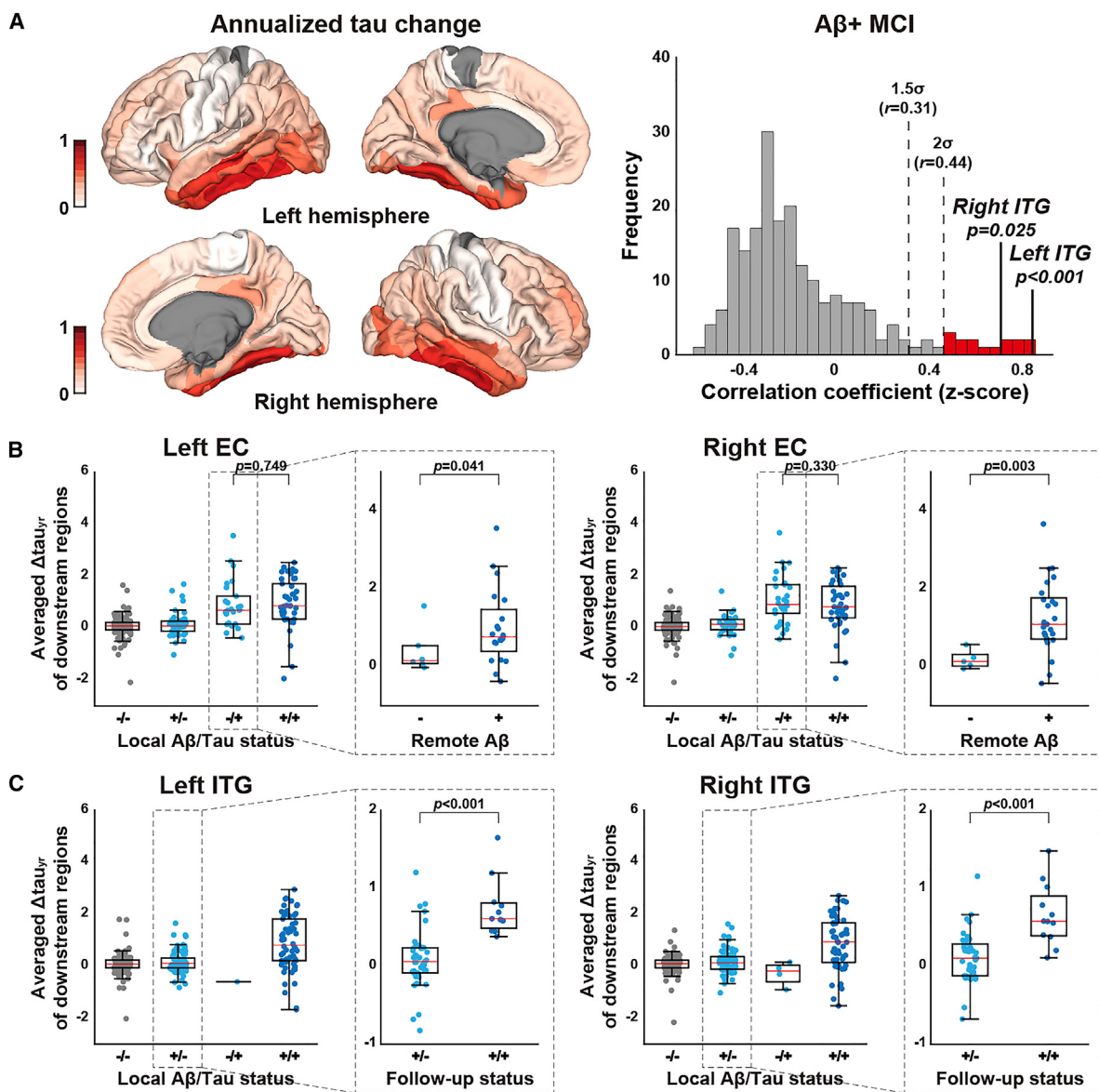


Figure 5. Longitudinal support for the network-based A_β-tau interaction model

(A) In A_β+ MCI subjects, tau-PET showed longitudinal tau accumulation in a regional pattern that strongly correlated with the network flow-based connectivity maps of the ITG propagation hubs. Correlation coefficients describing the relationship between each brain region's connectivity map and the A_β+ MCI tau accumulation map were converted to Z-scores and used to form a null hypothesis distribution; one-tailed p values were computed for the two ITG hubs. The red bars in the histogram show correlation coefficients more than 2 SD greater than the mean.

(B and C) The A_β-tau interaction model was assessed longitudinally with the EC and ITG using the entire longitudinal dataset. For the EC (B), the subjects were classified into 4 subgroups according to the status of each region with respect to local A_β and tau at baseline. In subjects with tau in the EC at baseline, local EC A_β showed no effect on tau spreading (two sample t tests, p value > 0.05). In subjects who lacked EC A_β, however, those with remote, connectivity-based A_β-tau interaction showed dramatically higher tau spreading than those without (Mann-Whitney U test, one tailed p value < 0.05; B, inset). By contrast, for the ITG regions (C), a transition to local A_β-tau interaction was associated with significantly greater longitudinal tau accumulation in downstream regions (Mann-Whitney U test, p value < 0.05; C, inset). Boxplot whiskers represent 1.5 times the interquartile range beyond the first and third quartiles. MCI, mild cognitive impairment; ITG, inferior temporal gyrus; EC, entorhinal cortex; Δτ_{yr}, annualized tau accumulation rate; PET, positron emission tomography; SD, standard deviation.

Next, to test the longitudinal predictions arising from the A_β-tau interaction components of our model, we established quantitative thresholds for A_β- and tau-PET positivity within each region brain-wide (see [STAR Methods](#)). We then used these thresholds to group subjects, irrespective of their clinical

label, based on their baseline A_β and tau status in the bilateral EC and ITG regions of interest previously identified through the cross-sectional remote and local A_β-tau interaction analyses. We quantified tau spreading into downstream regions by averaging the annualized tau accumulation rates within the 30

regions downstream of the regions of interest, based on the established tau spreading order ([Figure 1C; Table S1](#)). For the EC, we predicted that downstream tau spreading would be greatest when the EC is tau-positive at baseline, with little influence by the local co-presence of A β . Critically, however, our model predicts that regions downstream of the EC will show greater tau accumulation insofar as the EC is subjected to remote A β -tau interaction. Each of these EC-based predictions was supported by our longitudinal data ([Figure 5B](#); $t: 0.32/-0.98$, p value: $0.749/0.330$, left/right EC, for influence of local A β ; Mann-Whitney U test $Z: 1.73/2.73$, one-tailed p value: $0.041/0.003$, left/right EC; for influence of remote A β ; [Figure 5B](#) inset). Regarding the ITG propagation hubs, our model predicts accelerated tau spreading when A β and tau interact locally within the ITG. Here, we found that regions downstream of the ITG accumulated more tau in subjects who transitioned from having only A β in the ITG to having both A β and tau ([Figure 5C](#), inset; Mann-Whitney U test $Z: 4.23/4.04$, p value: $<0.001<0.001$, left/right ITG, for the influence of emerging A β -tau co-positivity). Emergent A β -tau co-positivity in the ITG was invariably the result of an A β -positive ITG that became tau-positive at follow-up. The longitudinal EC and ITG findings reported here were stable across a range of downstream region numbers ([Table S6](#)).

Two pivotal A β -tau interactions in the natural history of AD

The findings outlined above suggest two major inflection points in the molecular-anatomical pathogenesis of AD. The first occurs when neocortical A β emerges within multiple neocortical and limbic regions connected to the entorhinal cortices. This remote, connectivity-mediated interaction between A β and EC tau may induce tau to undergo biophysical changes that propel it to spread out of the entorhinal areas and into nearby, connected regions in the hippocampus, amygdala, and basal temporal cortices. The second pivotal moment occurs when tau neurofibrillary changes reach the ITG, where tau can locally interact, for the first time, with pre-existing A β , catalyzing widespread tau propagation into A β -positive and ITG-connected neocortical regions whose degeneration ultimately gives rise to dementia ([Sepulcre et al., 2018](#)). If these A β -tau interactions occur in sequence, as we hypothesize, then metrics capturing these two phenomena should obey a nonlinear relationship in which the EC remote A β -tau interaction rises first, before giving way to a rise in local A β -tau interaction within the ITG ([Figure 6A](#); see [STAR Methods](#)). Plotting these metrics across our discovery and validation cohorts, using cross-sectional and longitudinal data, strongly supported this prediction, demonstrating a fundamental arc of disease progression across and within individuals ([Figure 6B](#)). Quadratic regression models based on the mean (left/right) cross-sectional values fit both datasets well (ADNI: $R^2 = 0.664$, Korean: $R^2 = 0.652$), significantly better than did linear functions (ADNI: $R^2 = 0.658 / F$ [testing for the difference between quadratic and linear fit] = 7.022 , $p = 0.008$; Korean: $R^2 = 0.541 / F = 108.02$, $p = 2e-16$) ([Indrayan and Malhotra, 2017](#)). Focusing these analyses on subjects with at least one APOE $\epsilon 4$ allele further emphasized the nonlinear relationship (ADNI: $R^2 = 0.748 / F$ [testing for the difference between quadratic and linear fit] = 8.042 , $p = 0.005$; Korean:

$R^2 = 0.630 / F = 26.83$, $p = 1e-6$), perhaps because APOE $\epsilon 4$ carriers more often develop a typical anatomical progression that begins in medial temporal lobe memory structures ([Wolk et al., 2010](#)).

Based on the two pivotal A β -tau interactions, we stratified subjects into one of four groups: (1) “tau-negative” in EC; (2) insufficient EC remote A β -tau interaction to promote tau spreading (“latent tau”); (3) sufficient EC remote A β -tau interaction but minimal ITG local A β -tau interaction (“spreading tau”); and (4) sufficient ITG local A β -tau interaction (“propagating tau”). [Figure 6C](#) shows subject stratification assignments overlaid on the pseudo-longitudinal subject order derived from the tau frequency distribution approach. Using this stratification method, subjects assigned to the “spreading tau” group are found just before or shortly after the start of the tau acceleration phase, whereas those designated “propagating tau” are nearly all found within and beyond the acceleration phase. As expected, longitudinal subjects within the “spreading” and, in particular, “propagating” tau groups showed dramatically greater whole-brain annualized tau accumulation ([Figure 6D](#)). Expert recommendations for the use of the amyloid-lowering drug, aducanumab, emphasize the importance of positive AD biomarkers and a clinical label of MCI or mild dementia ([Cummings and Salloway, 2021](#)). Therefore, it is important to note that the model-driven subject stratification method presented here overlays inconsistently on the biomarker-anchored clinical groupings conventionally used in AD clinical trials ([Figure 6E; Table S7](#)). For example, subjects in the “spreading tau” group, whom we hypothesize will benefit most from amyloid-lowering therapy, represent only 14.4% of the overall A β + MCI group. These findings raise the possibility that a molecular-anatomical definition of disease stage may outperform clinical labels in predicting clinical responsiveness to amyloid-lowering and other AD therapies.

DISCUSSION

For decades, AD researchers have questioned how remote A β can stimulate neurofibrillary tauopathy to spread beyond the medial temporal lobe during the preclinical stages of AD ([Musiek and Holtzman, 2012; Jagust, 2018](#)). The present work shows that these early A β -tau interactions are likely mediated, at least in part, by long-range neural connections between the EC and brain regions in which early A β deposition occurs. More recent neuroimaging studies have emphasized a tau acceleration phase, in which frontal, temporal, and parietal heteromodal association cortex tauopathy takes hold in patients with late MCI, heralding the transition to dementia ([Sanchez et al., 2021a, 2021b](#)). Our findings identify the bilateral ITG regions as key propagation hubs whose connectional profiles are poised to disseminate tau throughout the neocortex, perhaps facilitated by local A β -tau interactions.

Tau spreading mechanisms remain a focus of intensive study, and transneuronal spreading is but one among several proposed mechanisms. The present neuroimaging analyses, conducted at the spatial resolution of brain regions and major fiber pathways, were not designed to address all potential cellular mechanisms or to estimate their relative contributions. Rather, we worked from the assumption that transneuronal spreading makes at

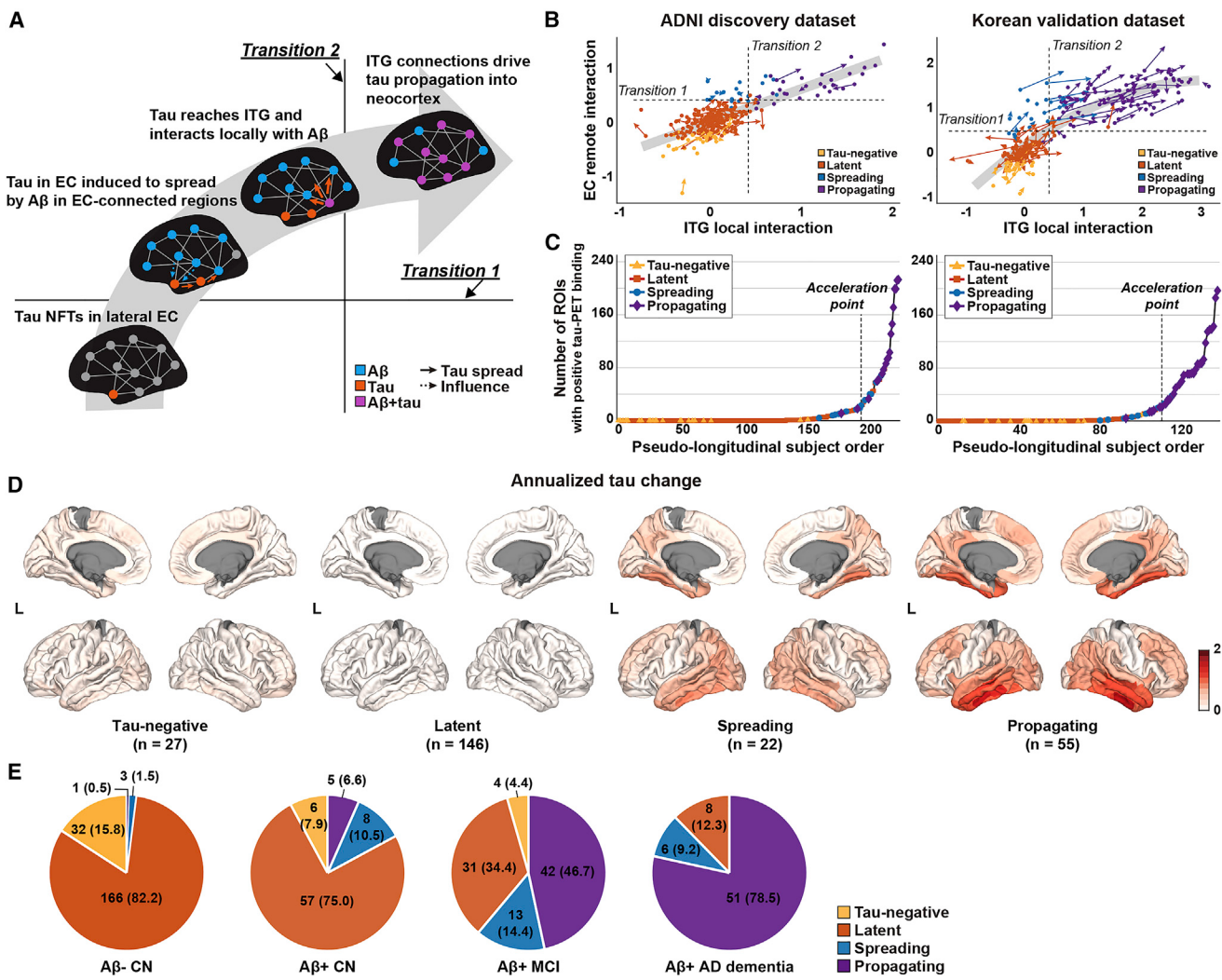


Figure 6. Two A β -tau interactions define a fundamental arc of AD molecular-anatomical progression

(A) Schematic representation of the AD progression model.

(B) Each subject's data are plotted, with an arrow connecting the baseline and follow-up scans (arrowhead points to later timepoint) where available. The nonlinear relationship between metrics representing EC remote A β -tau interaction and ITG local A β -tau interaction support the notion that these phenomena represent a temporal progression.

(C) Subjects were stratified into four groups and overlaid on the pseudo-longitudinal subject order derived from the tau frequency distribution approach. Group color-coding in (B) and (C) indicates four tau group assignments at baseline.

(D) Annualized longitudinal tau W-score change maps, stratified by baseline tau group assignment, demonstrate the dramatic increase in tau spreading in the propagating tau group.

(E) Subjects from the ADNI and Korean validation cohorts were stratified into 4 groups within each biomarker-anchored clinical label. EC, entorhinal cortex; ITG, inferior temporal gyrus; NFT, neurofibrillary tangle; ROI, region of interest; AD, Alzheimer's disease.

least some contribution to tau progression in AD even if other factors, such as shared regional vulnerability, local spreading, and other mechanisms contribute. In that regard, it is somewhat remarkable that a model based on transneuronal spreading provides such a strong fit to the experimental data. Nonetheless, not all of our findings fit the connectivity-based model. For example, not all participants with early AD conformed to the tau spreading pseudo-order derived from cross-sectional tau-PET data (Figure 1C). This variability may reflect heterogeneous AD anatomical trajectories (Vogel et al., 2021), connectivity-inde-

pendent tau spreading mechanisms, or a combination of these factors. Although our longitudinal data strongly supported the temporal predictions of our model, we observed some overlap in tau accumulation rates among patients who did or did not become newly co-positive for A β and tau in the ITG propagation hubs at follow-up (Figure 5C). This overlap could reflect involvement of non-ITG propagation hubs, PET tracer insensitivity to early tau deposition, or connectivity-independent tau progression. Additional research is needed to resolve these possibilities and to further refine the model proposed here.

A limitation of the current study is the use of a single structural connectome derived from healthy control subjects. Diffusion tensor imaging (DTI) tractography methods can result in erroneously estimated connections (Maier-Hein et al., 2017), and early-stage AD may alter the connectome in ways that could influence our model-based predictions. As in our previous work (Zhou et al., 2012; Brown et al., 2019), we used the normative connectome to model disease spreading based on the assumption that major changes in the fundamental connectome architecture are unlikely even if individual edge weights may be influenced by disease. Furthermore, we employed a network flow-based tau spreading model; this model reflects all possible paths between source and target regions, providing robustness to minor errors in single-edge connectivity estimation. A next step in the development of this model will be to incorporate individual patient functional and/or structural connectomes to evaluate whether and how disease-related connectivity changes modulate tau spreading.

Conclusion

Our findings address a long-standing question about the pathogenesis and progression of AD by placing early A β -tau interactions within a connectivity-based molecular-anatomical framework. This framework suggests that the natural history of AD traverses a critical period that begins once A β emerges within EC-connected regions, continues as tau spreads from the EC into connected mesial temporal and limbic regions, and may end once A β and tau interact within the ITG propagation hubs, whose connections are well suited to facilitate widespread neocortical tau propagation. The efficacy of A β -lowering drugs may depend on the timing of their delivery (Mintun et al., 2021), and the critical period defined here can now be evaluated as a potential therapeutic window. Additional work is needed to determine whether subject stratification methods based on this model can help predict responsiveness to A β -lowering and other AD therapeutic strategies.

STAR★METHODS

Detailed methods are provided in the online version of this paper and include the following:

- **KEY RESOURCES TABLE**
- **RESOURCE AVAILABILITY**
 - Lead contact
 - Materials availability
 - Data and code availability
- **EXPERIMENTAL MODEL AND SUBJECT DETAILS**
 - Participants
- **METHOD DETAILS**
 - Image acquisition
 - PET image processing
 - Structural network construction
- **QUANTIFICATION AND STATISTICAL ANALYSIS**
 - Determination of individual tau-PET pattern
 - Determination of pseudo-longitudinal order
 - Network flow-based connectivity derivation

- Propagation hub identification
- Statistical evaluation of network spread
- Analysis of network-based A β -tau interactions
- Longitudinal analyses of tau acceleration
- Network model-based subject stratification

SUPPLEMENTAL INFORMATION

Supplemental information can be found online at <https://doi.org/10.1016/j.neuron.2022.03.034>.

ACKNOWLEDGMENTS

Data collection and sharing for this project was funded by the Alzheimer's Disease Neuroimaging Initiative (ADNI) (National Institutes of Health grant U01 AG024904) and DOD ADNI (Department of Defense award number W81XWH-12-2-0012). ADNI is funded by the National Institute on Aging, the National Institute of Biomedical Imaging and Bioengineering, and through generous contributions from the following: AbbVie; Alzheimer's Association; Alzheimer's Drug Discovery Foundation; Araclon Biotech; BioClinica, Inc.; Biogen; Bristol-Myers Squibb Company; CereSpir, Inc.; Cogstate; Eisai Inc.; Elan Pharmaceuticals, Inc.; Eli Lilly and Company; EuroImmun; F. Hoffmann-La Roche Ltd and its affiliated company Genentech, Inc.; Fujirebio; GE Healthcare; IXICO Ltd.; Janssen Alzheimer Immunotherapy Research & Development, LLC; Johnson & Johnson Pharmaceutical Research & Development LLC; Lumosity; Lundbeck; Merck & Co., Inc.; Meso Scale Diagnostics, LLC; NeuroRx Research; Neurotrack Technologies; Novartis Pharmaceuticals Corporation; Pfizer Inc.; Piramal Imaging; Servier; Takeda Pharmaceutical Company; and Transition Therapeutics. The Canadian Institutes of Health Research is providing funds to support ADNI clinical sites in Canada. Private sector contributions are facilitated by the Foundation for the National Institutes of Health (www.fnih.org). The grantee organization is the Northern California Institute for Research and Education, and the study is coordinated by the Alzheimer's Therapeutic Research Institute at the University of Southern California. ADNI data are disseminated by the Laboratory of Neuro Imaging at the University of Southern California.

This work was partly supported by the National Research Foundation of Korea (NRF) grant funded by the Korean Government (MSIP) (no. 2019R1A2C109021211, NRF2020R1F1A1076154, NRF2020R1C1014725, & NRF2018R1D1A1B07049386), Yonsei University College of Medicine grant 6-2021-0094, the Institute of Information & Communications Technology Planning & Evaluation (IITP) grant funded by the Korean Government (MSIT) (no. 2019-0-00079, Department of Artificial Intelligence [Korea University]), Korea Health Industry Development Institute (HU20C0164), and by NIH grants AG019724, AG062422, AG055698, and AG065501.

AUTHOR CONTRIBUTIONS

W.J.L., J.-K.S., and W.W.S. conceived and designed the study. W.J.L., H.R.K., H.C., and C.H.L. contributed to data acquisition and processing. W.J.L. performed the experimental work, and W.J.L., J.A.B., J.-K.S., and W.W.S. analyzed and interpreted the results. W.J.L., J.A.B., J.-K.S., and W.W.S. wrote the manuscript, and J.-K.S. and W.W.S. substantively revised it. All authors participated in the discussion and critically reviewed the paper.

DECLARATION OF INTERESTS

W.W.S. received compensation as a lecturer for Corcept Therapeutics and as a consultant for Guidepoint Global Consulting and GLG Council. G.D.R. receives research support from the National Institutes of Health, Alzheimer's Association, American College of Radiology, Rainwater Charitable Foundation, gift from Edward and Pearl Fein, Avid Radiopharmaceuticals, Eli Lilly, Life Molecular Imaging, GE Healthcare, and Genentech. He has served as a consultant for Axon Neurosciences, Eisai, GE Healthcare, Merck, Genentech, and Roche. He serves on a data safety monitoring board for Johnson & Johnson.

He is an Associate Editor for JAMA Neurology. A subset of the authors has filed provisional patent no. 63/085,749 in the U.S. based on this work.

Received: November 18, 2021

Revised: February 19, 2022

Accepted: March 28, 2022

Published: April 19, 2022

REFERENCES

- Aizenstein, H.J., Nebes, R.D., Saxton, J.A., Price, J.C., Mathis, C.A., Tsopelas, N.D., Ziolkowski, S.K., James, J.A., Snitz, B.E., Houck, P.R., et al. (2008). Frequent amyloid deposition without significant cognitive impairment Among the elderly. *Arch. Neurol.* **65**, 1509–1517.
- Albert, M.S., Dekosky, S.T., Dickson, D., Dubois, B., Feldman, H.H., Fox, N.C., Gamst, A., Holtzman, D.M., Jagust, W.J., Petersen, R.C., et al. (2011). The diagnosis of mild cognitive impairment due to Alzheimer's disease: recommendations from the National Institute on Aging-Alzheimer's Association workgroups on diagnostic guidelines for Alzheimer's disease. *Alzheimers Dement.* **7**, 270–279.
- Baek, M.S., Cho, H., Lee, H.S., Choi, J.Y., Lee, J.H., Ryu, Y.H., Lee, M.S., and Lyoo, C.H. (2020). Temporal trajectories of in vivo tau and amyloid- β accumulation in Alzheimer's disease. *Eur. J. Nucl. Med. Mol. Imaging* **47**, 2879–2886.
- Beaulieu, C. (2002). The basis of anisotropic water diffusion in the nervous system – a technical review. *NMR Biomed.* **15**, 435–455.
- Benjamini, Y., and Hochberg, Y. (1995). Controlling the false discovery rate: A practical and powerful approach to multiple testing. *J. R. Stat. Soc. B Methodol.* **57**, 289–300.
- Braak, H., Alafuzoff, I., Arzberger, T., Kretschmar, H., and Del Tredici, K. (2006). Staging of Alzheimer disease-associated neurofibrillary pathology using paraffin sections and immunocytochemistry. *Acta Neuropathol.* **112**, 389–404.
- Braak, H., and Braak, E. (1991). Neuropathological staging of Alzheimer-related changes. *Acta Neuropathol.* **82**, 239–259.
- Braak, H., and Del Tredici, K. (2011). Alzheimer's pathogenesis: is there neuron-to-neuron propagation? *Acta Neuropathol.* **121**, 589–595.
- Brown, J.A., Deng, J., Neuhaus, J., Sible, I.J., Sias, A.C., Lee, S.E., Kornak, J., Marx, G.A., Karydas, A.M., Spina, S., et al. (2019). Patient-tailored, connectivity-based forecasts of spreading brain atrophy. *Neuron* **104**, 856–868.e5.
- Cho, H., Choi, J.Y., Hwang, M.S., Kim, Y.J., Lee, H.M., Lee, H.S., Lee, J.H., Ryu, Y.H., Lee, M.S., and Lyoo, C.H. (2016). In vivo cortical spreading pattern of tau and amyloid in the Alzheimer disease spectrum. *Ann. Neurol.* **80**, 247–258.
- Cho, H., Choi, J.Y., Lee, H.S., Lee, J.H., Ryu, Y.H., Lee, M.S., Jack, C.R., and Lyoo, C.H. (2019). Progressive tau accumulation in Alzheimer disease: 2-year follow-up study. *J. Nucl. Med.* **60**, 1611–1621.
- Choi, J.Y., Cho, H., Ahn, S.J., Lee, J.H., Ryu, Y.H., Lee, M.S., and Lyoo, C.H. (2018). Off-target 18F-AV-1451 binding in the basal ganglia correlates with age-related iron accumulation. *J. Nucl. Med.* **59**, 117–120.
- Clavaguera, F., Akatsu, H., Fraser, G., Crowther, R.A., Frank, S., Hench, J., Probst, A., Winkler, D.T., Reichwald, J., Staufenbiel, M., et al. (2013). Brain homogenates from human tauopathies induce tau inclusions in mouse brain. *Proc. Natl. Acad. Sci. USA* **110**, 9535–9540.
- Crary, J.F., Trojanowski, J.Q., Schneider, J.A., Abisambra, J.F., Abner, E.L., Alafuzoff, I., Arnold, S.E., Attems, J., Beach, T.G., Bigio, E.H., et al. (2014). Primary age-related tauopathy (PART): a common pathology associated with human aging. *Acta Neuropathol.* **128**, 755–766.
- Cummings, J., and Salloway, S. (2021). Aducanumab: appropriate use recommendations. *Alzheimers Dement.* **18**, 531–533.
- Das, S.R., Xie, L., Wisse, L.E.M., Ittyerah, R., Tustison, N.J., Dickerson, B.C., Yushkevich, P.A., and Wolk, D.A.; Alzheimer's Disease Neuroimaging Initiative. (2018). Longitudinal and cross-sectional structural magnetic resonance imaging correlates of AV-1451 uptake. *Neurobiol. Aging* **66**, 49–58.
- Ewing-Cobbs, L., Hasan, K.M., Prasad, M.R., Kramer, L., and Bachevalier, J. (2006). Corpus callosum diffusion anisotropy correlates with neuropsychological outcomes in twins discordant for traumatic brain injury. *AJNR Am. J. Neuroradiol.* **27**, 879–881.
- Fan, L., Li, H., Zhuo, J., Zhang, Y., Wang, J., Chen, L., Yang, Z., Chu, C., Xie, S., Laird, A.R., et al. (2016). The human Brainnetome atlas: A new brain atlas based on connectional architecture. *Cereb. Cortex* **26**, 3508–3526.
- Franzmeier, N., Neitzel, J., Rubinski, A., Smith, R., Strandberg, O., Ossenkoppelaar, R., Hansson, O., Ewers, M., and Alzheimer's Disease Neuroimaging Initiative (ADNI). (2020). Functional brain architecture is associated with the rate of tau accumulation in Alzheimer's disease. *Nat. Commun.* **11**, 347.
- Gold, B.T., Powell, D.K., Xuan, L., Jiang, Y., and Hardy, P.A. (2007). Speed of lexical decision correlates with diffusion anisotropy in left parietal and frontal white matter: evidence from diffusion tensor imaging. *Neuropsychologia* **45**, 2439–2446.
- Grothe, M.J., Barthel, H., Sepulcre, J., Dyrba, M., Sabri, O., and Teipel, S.J.; Alzheimer's Disease Neuroimaging Initiative. (2017). In vivo staging of regional amyloid deposition. *Neurology* **89**, 2031–2038.
- He, Z., Guo, J.L., McBride, J.D., Narasimhan, S., Kim, H., Changolkar, L., Zhang, B., Gathagan, R.J., Yue, C., Dengler, C., Stieber, A., et al. (2018). Amyloid-beta plaques enhance Alzheimer's brain tau-seeded pathologies by facilitating neuritic plaque tau aggregation. *Nat. Med.* **24**, 29–38.
- Hoaglin, D.C., Mosteller, F., and Tukey, J.W. (2000). Understanding Robust and Exploratory Data Analysis (Wiley).
- Hyman, B.T., Damasio, A.R., Van Hoesen, G.W., and Barnes, C.L. (1984). Alzheimer's disease: cell-specific pathology isolates the hippocampal formation. *Science* **225**, 1168–1170.
- Indrayan, A., and Malhotra, R.K. (2017). Medical Biostatistics (CRC Press).
- Iturria-Medina, Y., Sotero, R.C., Toussaint, P.J., and Evans, A.C.; Alzheimer's Disease Neuroimaging Initiative. (2014). Epidemic spreading model to characterize misfolded proteins propagation in aging and associated neurodegenerative disorders. *PLoS Comput. Biol.* **10**, e1003956.
- Jack, C.R., Knopman, D.S., Jagust, W.J., Shaw, L.M., Aisen, P.S., Weiner, M.W., Petersen, R.C., and Trojanowski, J.Q. (2010). Hypothetical model of dynamic biomarkers of the Alzheimer's pathological cascade. *Lancet Neurol.* **9**, 119–128.
- Jack, C.R., Petersen, R.C., Xu, Y.C., Waring, S.C., O'Brien, P.C., Tangalos, E.G., Smith, G.E., Ivnik, R.J., and Kokmen, E. (1997). Medial temporal atrophy on MRI in normal aging and very mild Alzheimer's disease. *Neurology* **49**, 786–794.
- Jagust, W. (2018). Imaging the evolution and pathophysiology of Alzheimer disease. *Nat. Rev. Neurosci.* **19**, 687–700.
- Jagust, W.J., Landau, S.M., Koeppe, R.A., Reiman, E.M., Chen, K., Mathis, C.A., Price, J.C., Foster, N.L., and Wang, A.Y. (2015). The Alzheimer's disease neuroimaging initiative 2 PET core: 2015. *Alzheimers Dement.* **11**, 757–771.
- Johnson, K.A., Schultz, A., Betensky, R.A., Becker, J.A., Sepulcre, J., Rentz, D., Mormino, E., Chhatwal, J., Amariglio, R., Papp, K., et al. (2016). Tau positron emission tomographic imaging in aging and early Alzheimer disease. *Ann. Neurol.* **79**, 110–119.
- Joshi, A.D., Pontecorvo, M.J., Clark, C.M., Carpenter, A.P., Jennings, D.L., Sadowsky, C.H., Adler, L.P., Kovnat, K.D., Seibyl, J.P., Arora, A., et al. (2012). Performance characteristics of amyloid PET with florbetapir F 18 in patients with Alzheimer's disease and cognitively normal subjects. *J. Nucl. Med.* **53**, 378–384.
- Kim, E.J., Hwang, J.L., Gaus, S.E., Nana, A.L., Deng, J., Brown, J.A., Spina, S., Lee, M.J., Ramos, E.M., Grinberg, L.T., et al. (2020). Evidence of corticofugal tau spreading in patients with frontotemporal dementia. *Acta Neuropathol.* **139**, 27–43.
- La Joie, R., Perrotin, A., Barré, L., Hommet, C., Mëzenge, F., Ibazizene, M., Camus, V., Abbas, A., Landeau, B., and Guilloteau, D. (2012). Region-specific hierarchy between atrophy, hypometabolism, and β -amyloid ($A\beta$) load in Alzheimer's disease dementia. *J. Neurosci.* **32**, 16265–16273.

- Lemoine, L., Leuzy, A., Chiotis, K., Rodriguez-Vieitez, E., and Nordberg, A. (2018). Tau positron emission tomography imaging in tauopathies: the added hurdle of off-target binding. *Alzheimers. Dement. (Amst)* **10**, 232–236.
- Leuzy, A., Chiotis, K., Lemoine, L., Gillberg, P.G., Almkvist, O., Rodriguez-Vieitez, E., and Nordberg, A. (2019). Tau PET imaging in neurodegenerative tauopathies—still a challenge. *Mol. Psychiatry* **24**, 1112–1134.
- Liu, L., Drouet, V., Wu, J.W., Witter, M.P., Small, S.A., Clelland, C., and Duff, K. (2012). Trans-synaptic spread of tau pathology in vivo. *PLoS One* **7**, e31302.
- Lockhart, S.N., Ayakta, N., Winer, J.R., La Joie, R., Rabinovici, G.D., and Jagust, W.J. (2017). Elevated (18)F-AV-1451 PET tracer uptake detected in incidental imaging findings. *Neurology* **88**, 1095–1097.
- Maass, A., Landau, S., Baker, S.L., Horng, A., Lockhart, S.N., La Joie, R., Rabinovici, G.D., and Jagust, W.J.; Alzheimer's Disease Neuroimaging Initiative. (2017). Comparison of multiple tau-PET measures as biomarkers in aging and Alzheimer's disease. *NeuroImage* **157**, 448–463.
- Maier-Hein, K.H., Neher, P.F., Houde, J.-C., Côté, M.-A., Garyfallidis, E., Zhong, J., Chamberland, M., Yeh, F.-C., Lin, Y.-C., Ji, Q., et al. (2017). The challenge of mapping the human connectome based on diffusion tractography. *Nat. Commun.* **8**, 1349.
- McDade, E., Wang, G., Gordon, B.A., Hassenstab, J., Benzinger, T.L.S., Buckles, V., Fagan, A.M., Holtzman, D.M., Cairns, N.J., Goate, A.M., et al. (2018). Longitudinal cognitive and biomarker changes in dominantly inherited Alzheimer disease. *Neurology* **91**, e1295–e1306.
- McKhann, G.M., Knopman, D.S., Chertkow, H., Hyman, B.T., Jack, C.R., Kawas, C.H., Klunk, W.E., Koroshetz, W.J., Manly, J.J., Mayeux, R., et al. (2011). The diagnosis of dementia due to Alzheimer's disease: recommendations from the National Institute on Aging-Alzheimer's Association workgroups on diagnostic guidelines for Alzheimer's disease. *Alzheimers. Dement.* **7**, 263–269.
- Mintun, M.A., Lo, A.C., Duggan Evans, C., Wessels, A.M., Ardayfio, P.A., Andersen, S.W., Shcherbinin, S., Sparks, J., Sims, J.R., Brys, M., et al. (2021). Donanemab in early Alzheimer's disease. *N. Engl. J. Med.* **384**, 1691–1704.
- Musiek, E.S., and Holtzman, D.M. (2012). Origins of Alzheimer's disease: reconciling cerebrospinal fluid biomarker and neuropathology data regarding the temporal sequence of amyloid-beta and tau involvement. *Curr. Opin. Neurol.* **25**, 715–720.
- Ossenkoppelaar, R., Iaccarino, L., Schonhaut, D.R., Brown, J.A., La Joie, R., O'Neil, J.P., Janabi, M., Baker, S.L., Kramer, J.H., Gorno-Tempini, M.L., et al. (2019). Tau covariance patterns in Alzheimer's disease patients match intrinsic connectivity networks in the healthy brain. *NeuroImage Clin.* **23**, 101848.
- Ossenkoppelaar, R., Pijnenburg, Y.A., Perry, D.C., Cohn-Sheehy, B.I., Scheltens, N.M., Vogel, J.W., Kramer, J.H., Van Der Vlies, A.E., La Joie, R.L., Rosen, H.J., et al. (2015). The behavioural/dysexecutive variant of Alzheimer's disease: clinical, neuroimaging and pathological features. *Brain* **138**, 2732–2749.
- Petersen, R.C., Aisen, P.S., Beckett, L.A., Donohue, M.C., Gamst, A.C., Harvey, D.J., Jack, C.R., Jagust, W.J., Shaw, L.M., Toga, A.W., et al. (2010). Alzheimer's Disease Neuroimaging Initiative (ADNI): clinical characterization. *Neurology* **74**, 201–209.
- Raj, A., Kuceyeski, A., and Weiner, M. (2012). A network diffusion model of disease progression in dementia. *Neuron* **73**, 1204–1215.
- Raj, A., Locastro, E., Kuceyeski, A., Tosun, D., Relkin, N., Weiner, M., and Alzheimer's Disease Neuroimaging Initiative (ADNI). (2015). Network diffusion model of progression predicts longitudinal patterns of atrophy and metabolism in Alzheimer's disease. *Cell Rep.* **10**, 359–369.
- Sanchez, J.S., Becker, J.A., Jacobs, H.I.L., Hanseeuw, B.J., Jiang, S., Schultz, A.P., Properzi, M.J., Katz, S.R., Beiser, A., Satizabal, C.L., et al. (2021a). The cortical origin and initial spread of medial temporal tauopathy in Alzheimer's disease assessed with positron emission tomography. *Sci. Transl. Med.* **13**, eabc0655.
- Sanchez, J.S., Hanseeuw, B.J., Lopera, F., Sperling, R.A., Baena, A., Bocanegra, Y., Aguillon, D., Guzmán-Vélez, E., Pardilla-Delgado, E., Ramirez-Gomez, L., et al. (2021b). Longitudinal amyloid and tau accumulation in autosomal dominant Alzheimer's disease: findings from the Colombia-Boston (COLBOS) biomarker study. *Alzheimer's Res. Therapy* **13**, 27.
- Scott, M.R., Hampton, O.L., Buckley, R.F., Chhatwal, J.P., Hanseeuw, B.J., Jacobs, H.I.L., Properzi, M.J., Sanchez, J.S., Johnson, K.A., Sperling, R.A., et al. (2020). Inferior temporal tau is associated with accelerated prospective cortical thinning in clinically normal older adults. *NeuroImage* **220**, 116991.
- Sepulcre, J., Grothe, M.J., D'Oleire Uquillas, F., Ortiz-Terán, L., Diez, I., Yang, H.S., Jacobs, H.I.L., Hanseeuw, B.J., Li, Q., El-Fakhri, G., et al. (2018). Neurogenetic contributions to amyloid beta and tau spreading in the human cortex. *Nat. Med.* **24**, 1910–1918.
- Thal, D.R., Rüb, U., Orantes, M., and Braak, H. (2002). Phases of A beta-deposition in the human brain and its relevance for the development of AD. *Neurology* **58**, 1791–1800.
- Tsai, R.M., Bejanin, A., Lesman-Segev, O., Lajoie, R., Visani, A., Bourakova, V., O'Neil, J.P., Janabi, M., Baker, S., Lee, S.E., et al. (2019). 18F-flortaucipir (AV-1451) tau PET in frontotemporal dementia syndromes. *Alzheimers Res. Ther.* **11**, 13.
- Van Den Heuvel, M.P., and Sporns, O. (2011). Rich-club organization of the human connectome. *J. Neurosci.* **31**, 15775–15786.
- Vogel, J.W., Iturria-Medina, Y., Strandberg, O.T., Smith, R., Levitis, E., Evans, A.C., and Hansson, O.; Alzheimer's Disease Neuroimaging Initiative; Swedish BioFinder Study (2020). Spread of pathological tau proteins through communicating neurons in human Alzheimer's disease. *Nat. Commun.* **11**, 2612.
- Vogel, J.W., Young, A.L., Oxtoby, N.P., Smith, R., Ossenkoppelaar, R., Strandberg, O.T., La Joie, R., Aksman, L.M., Grothe, M.J., Iturria-Medina, Y., et al. (2021). Four distinct trajectories of tau deposition identified in Alzheimer's disease. *Nat. Med.* **27**, 871–881.
- Wang, R., Benner, T., Sorensen, A.G., and Wedeen, V.J. (2007). Diffusion toolkit: a software package for diffusion imaging data processing and tractography. *Proc. Int. Soc. Magn. Reson. Med.* **15**, 3720.
- Waters, J. (2010). The concentration of soluble extracellular amyloid- β protein in acute brain slices from CRND8 mice. *PLoS One* **5**, e15709.
- Wilson, R.J. (1979). Introduction to Graph Theory (Pearson Education).
- Wolk, D.A., and Dickerson, B.C.; Alzheimer's Disease Neuroimaging Initiative (2010). Apolipoprotein E (APOE) genotype has dissociable effects on memory and attentional-executive network function in Alzheimer's disease. *Proc. Natl. Acad. Sci. USA* **107**, 10256–10261.
- Wook Yoo, S., Han, C.E., Shin, J.S., Won Seo, S., Na, D.L., Kaiser, M., Jeong, Y., and Seong, J.K. (2015). A network flow-based analysis of cognitive reserve in normal ageing and Alzheimer's disease. *Sci. Rep.* **5**, 10057.
- Zhou, J., Gennatas, E.D., Kramer, J.H., Miller, B.L., and Seeley, W.W. (2012). Predicting regional neurodegeneration from the healthy brain functional connectome. *Neuron* **73**, 1216–1227.

STAR★METHODS

KEY RESOURCES TABLE

REAGENT or RESOURCE	SOURCE	IDENTIFIER
Deposited data		
Raw and analyzed data	ADNI	http://adni.loni.usc.edu/
Brainnetome atlas	Fan et al. (2016)	http://www.brainnetome.org/
Software and algorithms		
MATLAB	Mathworks	https://www.mathworks.com/
FreeSurfer	Open source	http://surfer.nmr.mgh.harvard.edu/
FSL	FMRIB	https://fsl.fmrib.ox.ac.uk/fsl/
UCLA Multimodal Connectivity Package		https://github.com/jbrown81/umcp/
Custom MATLAB code		https://github.com/wjlee3/neuron_2022 https://doi.org/10.5281/zenodo.6387082

RESOURCE AVAILABILITY

Lead contact

Further information and requests for resources should be directed to and will be fulfilled by the lead contact, William Seeley (bill.seeley@ucsf.edu).

Materials availability

This study did not generate new unique reagents.

Data and code availability

All data reported in this paper will be shared by the [lead contact](#) upon request. All original code has been deposited at GitHub and is publicly available as of the date of publication. DOIs are listed in the [key resources table](#). Any additional information required to re-analyze the data reported in this paper is available from the [lead contact](#) upon request.

EXPERIMENTAL MODEL AND SUBJECT DETAILS

Participants

We included participants from two non-overlapping datasets for this study: the discovery dataset and the validation dataset. The discovery dataset consisted of participants from the Alzheimer's Disease Neuroimaging Initiative (ADNI, <http://adni.loni.usc.edu/>) and includes patients with AD-type dementia, mild cognitive impairment (MCI), and cognitively normal age-matched controls. All participants underwent structural magnetic resonance imaging (MRI) scans and positron emission tomography (PET) using ¹⁸F-florbetapir (AV45) for Aβ and ¹⁸F-flortaucipir (AV1451) scans for tau. 187 cognitively normal (CN) subjects, 64 patients with early MCI (early MCI), 30 patients with late MCI (late MCI), and 11 patients with AD dementia were used for the discovery dataset. Detailed diagnostic criteria were previously reported (<http://adni.loni.usc.edu/methods/>) (Petersen et al., 2010). Of the 292 subjects available, four CN subjects, one early MCI patient, and two AD-type dementia patients were excluded due to poor co-registration quality between MRI and PET scans. One early MCI patient and one CN subject were excluded due to poor pre-processing during Freesurfer-based image analysis. The ADNI sample size for the main analyses was 283 (Table 1). We also included 95 CN subjects from ADNI to construct the healthy structural connectome. These participants satisfied identical diagnostic criteria as the previous CN subjects but were chosen because they had undergone structural MRI scans and diffusion-weighted MRI (DWI) scans suitable for diffusion tractography. Of these 95 subjects, 49 were also included in the discovery dataset used for PET analysis.

The validation dataset included participants clinically diagnosed at Gangnam Severance Hospital, South Korea, from January 2015 to July 2016 (Table 1). This study was approved by the institutional review board of Gangnam Severance Hospital and written informed consent was obtained from all subjects. All participants in the validation dataset underwent structural MRI, as well as ¹⁸F-florbetaben PET for Aβ and ¹⁸F-flortaucipir PET for tau. The participants included 96 CN subjects showing normal performance on neuropsychological tests and no abnormalities on brain MRI, as well as 84 patients with amnestic MCI (aMCI) and 71 with AD-type dementia fulfilling the National Institute on Aging–Alzheimer Association diagnostic criteria for “MCI due to AD with intermediate or high likelihood” (Albert et al., 2011) and “probable dementia with evidence of the AD pathophysiologic process” (McKhann et al., 2011), respectively. Detailed diagnostic criteria for all three clinical groups have been described (Cho et al., 2019).

For longitudinal analyses, we downloaded additional image data from the ADNI repository in January 2021. All participants had baseline scans satisfying the same criteria used for the cross-sectional analyses and had undergone follow-up structural MRI and flortaucipir PET scans. Due to the limited samples available, we included all MCI subjects and considered early and late MCI together ([Table 1](#)). With 19 newly added subjects after excluding 4 due to image co-registration errors, 72 CN subjects, 55 patients with MCI (amyloid-PET-positive: 32), and 8 patients with AD dementia were available for the ADNI discovery dataset. In the Korean validation dataset, 169 participants including 74 CN subjects, 59 patients with amnestic MCI (amyloid-PET-positive: 36), and 36 patients with dementia (amyloid-PET-positive: 28) had follow-up scans. After calculating mean annualized change in tau-PET *W*-scores across all ROIs, four subjects with extreme outlier values, defined as any values more than 3 times the interquartile range above the third quartile, were removed from the longitudinal analyses ([Hoaglin et al., 2000](#)).

METHOD DETAILS

Image acquisition

For the discovery (ADNI) dataset, structural MRI and PET scans were downloaded on April 2019 from the ADNI repository. Structural MRIs were acquired in ADNI-2 and ADNI-3 phases using 3T MRI scanners with 3D magnetization-prepared rapid gradient echo (MP-RAGE) or inversion recovery-fast spoiled gradient recalled (IR-SPGR) sequences. Detailed protocols of MRI scanner for T₁-weighted imaging can be found online (<http://adni.loni.usc.edu/methods/documents/mri-protocols/>). Flortaucipir PET scans were acquired for 20 minutes (4 × 5 min frames) at 50–70 min post injection of 10 mCi tracers, and Flortaucipir PET scans were acquired for 30 min (6 × 5 min frames) at 75–105 min post injection of 10 mCi tracers. We only used MRI scans having the shortest interval between MRI and Flortaucipir PET acquisition, all within six months (37 ± 40 days) of each other. Flortaucipir images were used if acquired within 1 year of Flortaucipir (23 ± 38 days), in keeping with previous approaches ([Das et al., 2018](#); [Maass et al., 2017](#)). DWI had the same acquisition date as the corresponding T₁-weighted MRI. Multiple b=0 s/mm² images and 48 b=1000 s/mm² images were acquired for DWI with 2 × 2 × 2 mm³ voxels in ADNI-3 phase (<http://adni.loni.usc.edu/methods/>). In the validation (Korean) dataset, T₁-weighted MRI was also obtained using a 3T MR scanner with 3D SPGR sequence. Each of the Florbetaben and Flortaucipir PET scans was acquired for 20 minutes on separate days at 90 min and 80 minutes after the injection of tracers, respectively. Detailed acquisition parameters have been described ([Cho et al., 2019](#)).

PET image processing

Each Aβ- and tau-PET image for both baseline and follow-up scans was preprocessed as follows ([Vogel et al., 2021](#)). The raw PET image was first co-registered between frames to reduce motion effects with conversion to DICOM format and processed by averaging five-minute frames. The generated images were then reoriented into a standard 160 × 160 × 96 voxel image grid with 1.5 mm cubic voxels and intensity normalized. Finally, smoothing was performed with a scanner-specific filter function to make a uniform isotropic resolution of 8 mm full width at half maximum ([Jagust et al., 2015](#)) (<http://adni.loni.usc.edu/>). PET images were co-registered to the corresponding T₁ image using FMRIB Software Library (FSL) Linear Registration Tool (FLIRT). For each hemisphere, we used the atlas parcellation comprising 105 cerebral cortical and 18 subcortical brain regions defined by the Brainnetome atlas ([Fan et al., 2016](#)), which was reverse-normalized to each participant's structural MRI scan. Standardized uptake value ratio (SUVR) images were obtained using whole cerebellum as a reference region. The voxel values assigned to a previously identified region-of-interest (ROI) were averaged to obtain a regional SUVR value. The global retention ratio for Flortaucipir images was computed based on Aβ-related regions including the frontal, anterior/posterior cingulate, lateral parietal, and lateral temporal regions ([Jagust et al., 2015](#)). Subjects were classified as amyloid-positive when the global Flortaucipir retention ratio exceeded 1.11, consistent with previous approaches ([Joshi et al., 2012](#)) (<http://adni.loni.usc.edu/>).

Structural network construction

Structural networks were constructed using diffusion tensor imaging (DTI) techniques, based on eddy-current-corrected diffusion-weighted MR images (FSL, <http://www.fmrib.ox.ac.uk/fsl/>). Each structural network consisted of nodes (brain regions) and edges (connections between node pairs). For each hemisphere, the nodes comprised the 105 cerebral cortical and 18 subcortical brain regions defined by the Brainnetome atlas ([Fan et al., 2016](#)). T₁-weighted MR image volumes from the Brainnetome atlas were resampled to corresponding eddy-current-corrected diffusion-weighted MR image volumes using FreeSurfer (<http://surfer.nmr.mgh.harvard.edu/>) to specify the nodes of each structural network. We derived the structural connectivity matrix at both individual and group levels. An individual-level network edge was deemed present if there was at least one streamline between a node pair, acquired by whole-brain deterministic tractography using the second order Runge-Kutta algorithm through the Diffusion toolkit ([Wang et al., 2007](#)). Fiber tracking was initiated at the 8 random points of each seed voxel with a fractional anisotropy (FA) > 0.3 and ended at the voxels with FA < 0.2 or a tract turning angle of > 45 degrees. The strength of each edge was determined based on the FA values averaged across all connecting streamlines using the UCLA Multimodal Connectivity Package (<https://github.com/jbrown81/umcp>) ([van den Heuvel and Sporns, 2011](#)). FA values have been considered to represent the level of microstructural organization of white matter tracts ([Beaulieu, 2002](#)), which has been associated with the functional efficacy of the connections

(Ewing-Cobbs et al., 2006; Gold et al., 2007). The group-level network was computed by averaging individual network edges present in more than a third of all healthy (A β - CN) subjects. In the group-level network, 4.68% of edges were connected, and their range of mean FA values was 0.2215 [0.1766, 0.2842] (median [Q1, Q3]).

QUANTIFICATION AND STATISTICAL ANALYSIS

Determination of individual tau-PET pattern

We employed gaussian mixture modeling for each ROI to address off-target Flortaucipir binding (Choi et al., 2018; Lemoine et al., 2018; Lockhart et al., 2017). Following previous approaches (Vogel et al., 2020), we assumed that a distribution of pathological signal would be skewed while those of off-target and non-specific signals would remain normally distributed across the study sample. All Flortaucipir SUVR values of each ROI were fitted through a one-component and a two-component gaussian mixture model, of which the results were compared five times using Bayesian information criterion (BIC). Consistently lower BIC in a one-component model than a two-component model indicates SUVR values of the region are roughly normally distributed, implying no evidence of pathological tau deposition. The regions fitted better with a one-component model were considered as not or not yet involved in tauopathy, so not included in the study (33 brain regions were regarded as off-target regions for the ADNI dataset and 46 for the Korean validation dataset; see Table S2).

We then constructed a *W*-score map (Jack et al., 1997; La Joie et al., 2012; Ossenkoppele et al., 2015) for each Flortaucipir PET image to represent individual pathological tau burden compared to the amyloid-PET-negative CN group (Tsai et al., 2019). *W*-scores are standardized values adjusted for covariates including age, sex, and years of education. For each ROI, a linear regression was performed between the covariates and the regional SUVR values in the control group. The *W*-score was computed as a difference between actual and predicted pathological burden (i.e. the residual) of each subject, divided by the standard deviation of residuals in the control group. In the individual *W*-score maps generated for Flortaucipir PET scans, greater values indicate greater Flortaucipir uptake, suggesting greater tau pathological burden.

Determination of pseudo-longitudinal order

To study the non-linear acceleration of tau aggregation required the use of cross-sectional data to make longitudinal inferences. To this end, we first constructed a pseudo-longitudinal order by applying a frequency-based method to the tau-PET data of presymptomatic and prodromal AD (A β -positive CN and MCI, early or late) subjects. ROIs were ordered to define a regional tau spreading order by the frequencies with which the regional *W*-scores exceeded a given threshold across all subjects. We used a *W*-score threshold of 2.5, following previous research (Cho et al., 2016), but other thresholds were also considered to evaluate robustness (see Figure S1). Subjects were sorted based on their number of ROIs having suprathreshold tau *W*-scores. To determine the period in which tau acceleration occurs, we used a smoothed line of the frequency graph based on the pseudo-longitudinal order. We deemed that the acceleration phase begins where the slope of the graph becomes larger than two and ends at the second inflection point, where the second derivative become zero.

Network flow-based connectivity derivation

We constructed a flow-based network based on maximum inter-nodal flow, using the whole-brain structural network to model the extent of tau propagation between each node pair. Every possible non-overlapping distinct path between any two nodes was extracted by employing a graph-theoretical maximum-flow calculation method using the binary normative brain network (Wook Yoo et al., 2015; Wilson, 1979). Each separate path contributed to the total inter-nodal flow by the amount of the mean FA value of all edges in the path divided by the average inter-nodal streamline length in mm. The partial contributions were then combined through all distinct paths, which became an edge weight between the source and sink nodes in the flow-based connectivity matrix. By adopting multiple distinct paths between two nodes, the flow-based network provides a method for predicting the physical amount of tau delivered from the source to sink node. This flow network was constructed at both the individual and group levels using the healthy structural connectome.

Propagation hub identification

The flow-based network described above was next used to identify propagation hubs, hypothesized to drive the acceleration phase of tau spreading. To this end, we searched a library of network flow-based connectivity maps, one seeded by each of the 246 brain regions-of-interest, and we estimated the goodness-of-fit (GOF) of each seed's map to the progression of tau through the regions representing the tau acceleration phase. Specifically, binary inner and outer masks were defined within the tau acceleration phase regions across a range of thresholds (see Figure S3). Assuming that the propagation hubs template the topography of acceleration phase tau spreading, the inner and outer mask regions were constrained to tau acceleration phase regions, arranged using the pseudo-longitudinal regional tau spreading order. We assigned the first thirty brain regions to the inner mask and the next thirty regions to the outer mask to capture earlier and later tau spreading. The inner mask was then gradually expanded by ten regions, producing 7 different sets of inner-outer mask pairs (see Figure S3), to mimic tau propagation and to avoid potential influence of arbitrary thresholding. For example, the second mask set had the first forty regions as the inner mask and the next thirty regions as the outer mask. A GOF score was calculated for each seed by subtracting its average connectivity to the outer mask area

from its average connectivity to the inner mask area., and a permutation-based one-sample t-test was performed using the GOF scores. The significance level was determined using $p < 0.05$, Bonferroni-corrected for multiple tests. The propagation hubs were identified as the regions showing significant GOF scores for all 7 mask pairs. In this way, regions that show the highest and most robust connectivity to regions that become tau-positive early in the acceleration phase were selected as propagation hubs.

Statistical evaluation of network spread

To assess the relationship between the network flow-based connectivity in health and the topographical pattern of tau acceleration phase, we performed correlation analyses between the group-level flow network derived from the identified ITG propagation hubs and the group-level tau-PET W -score contrast maps from ADNI subjects. The tau-PET contrast map was obtained by averaging all possible two-subject tau-PET W -score difference maps from subjects drawn (one each) from the acceleration and pre-acceleration periods. The pre-acceleration period consists of subjects ordered before the acceleration phase, based on the pseudo-longitudinal subject order, insofar as they had at least one tau-positive region. Correlations were then evaluated in each hemisphere using the ipsilateral propagation hub. To place our findings in context of previous work from our group (Brown et al., 2019; Zhou et al., 2012), we compared the network flow-based correlations to those derived using shortest path length and Euclidean distance from the propagation hubs. The matrix of shortest path length was computed using group-level FA-weighted structural connectivity, and the Euclidean distances between each pair of nodes were averaged through all healthy subjects. For the correlation analyses, statistical significance was set to $p < 0.05$ and multiple comparisons were corrected using the Benjamini-Hochberg false discovery rate (FDR) method (Benjamini and Hochberg, 1995) across three different measures and the two ITG propagation hubs. Furthermore, we calculated the null distribution of z-transformed correlation coefficients using all brain regions as seeds to assess the statistical meaning of the correlation coefficient for the ITG propagation hubs compared to other regions in terms of correlation with the topographical tau deposition representing the acceleration > pre-acceleration phase pattern as defined above.

Analysis of network-based A β -tau interactions

We evaluated the relationship between A β and tau based on remote and local interactions. For computing remote interactions of each ROI, A β -PET SUVR values in each connected region, based on the structural connectome, were multiplied by the FA value of the connecting tract, inversely weighted by the streamline length, based on the notion that remote interactions will reflect the strength of the connection and the distance over which these effects must travel (Iturria-Medina et al., 2014; Waters, 2010). The connectivity-weighted A β -PET SUVRs for all connected regions were summed, and this remote A β influence value was then multiplied by the tau W -score of the ROI. In this way, a region's remote A β -tau interaction was determined by the strength and number of its connections to A β -PET-positive brain areas and by its local tau deposition. Similarly, local A β -tau interactions were obtained by multiplying the region's A β -PET SUVR by the region's local tau W -score. For the magnitude of A β deposition, the regional A β -PET SUVR value was used because of its narrow dynamic range; in this context, W -score normalization may skew or exaggerate small changes in A β deposition (Grothe et al., 2017).

To estimate where the remote and local interactions take place earliest in AD progression, we applied the same frequency-based method used for constructing the pseudo-longitudinal tau spreading order. Brain regions were ordered using the frequencies with which their remote or local A β influence metric was positive and the tau W -score exceeded a given threshold. Both remote A β influence and local A β positivity were determined using regional cutoff values calculated by employing a previously reported method (Aizenstein et al., 2008) that iteratively removes outliers within each region's data from the A β -negative CN group until no outlier arises and multiplies the maximum of remaining values by a small number as a buffer. We considered the values higher than $1.5 \times$ the interquartile range over the third quartile as outliers and identified a cutoff value as the 95th percentile of the remaining data after removing outliers. In addition, we compared the interaction score of each region with the median interaction scores of all other regions from the ipsilateral hemisphere. For this comparison, the continuous values of both interaction scores were used. To address regional variations in A β -PET SUVR across the whole brain, we normalized the remote/local A β influence using the regional cutoffs, which were multiplied by each ROI's local tau W -score to compute the remote and local A β -tau interaction scores. Permutation-based one-sample t-tests were used across all subjects and multiple comparisons were corrected using the FDR method (Benjamini and Hochberg, 1995) across all regions within each hemisphere. To verify robustness of the interaction pseudo-order, we also considered a range of tau thresholds (see Figure S6).

According to our hypotheses and main results (see Figure 4), we assumed that the remote A β -tau interactions occur earliest in the entorhinal cortex and have a critical influence on tau spreading from the EC, whereas local interactions occur early and crucially within the ITG. Therefore, we examined the location of the EC on the distribution of t-statistics for remote interaction scores and the inferior temporal gyrus on the distribution of t-statistics for local interaction scores (see Figures 4 and S7).

Longitudinal analyses of tau acceleration

To strengthen the statistical power of the longitudinal analyses, we used regional tau W -scores of the ADNI and Korean datasets together. First, to determine whether the connectivity of the ITG stands out as a predictor of longitudinal tau accumulation, we performed correlation analyses between the regional flow-based networks, derived from healthy controls, and the group-level annualized change in tau-PET W -maps, derived from A β + subjects with MCI ($n = 68$). Off-target regions co-occurring in both datasets were removed from the correlation analyses but retained in network flow-based map construction, in keeping with the cross-

sectional analyses. The correlation coefficients of all seed regions were transformed to z-scores, and the values of the ITG propagation hubs were presented on the distribution (see [Figure 5A](#)).

Next, to assess the relationship between the two key A β -tau interactions and longitudinal tau accumulation, subjects were stratified by the status of local A β and tau for each ROI separately (including both left and right EC and ITG) as follows: (1) both A β and tau were negative (-/-), (2) A β was positive while tau was negative (+/-), (3) A β was negative while tau was positive (-/+), and (4) both were positive (+/+). Necessarily, for each region-of-interest, groups 1–4 had different subject compositions. For each subject, we determined the tau accumulation rate in regions “downstream” to the region-of-interest, by averaging the annualized change rates across tau W-scores among the 30 regions immediately following the region-of-interest within the dataset-specific regional tau spreading order. We first performed two-sample t-tests using the averaged annualized change rates to compare the effects of the EC being A β -positive vs. A β -negative in the presence of local tau-positivity. For the EC, subjects with negative local A β and positive tau were further divided into two subgroups according to the EC remote A β -tau interaction status: remote A β -negative/local tau-positive and remote A β -positive/local tau-positive (see [Figure 5B](#)). The downstream tau accumulation rates of the two subgroups were compared to examine the effects of remote A β on tau within the EC, using a Mann-Whitney U test, appropriate here due to the nonparametric distribution of the tau accumulation rate in these subgroups. We next evaluated the effects of local interaction between A β and tau within the ITG ([Figure 5C](#)). Subjects lacking local tau while having positive A β within the ITG were further divided into two sub-groups based on whether tau positivity emerged in the ITG at follow-up. The rationale for this subgrouping was that it would allow us to determine whether arrival of tau at the (already A β -positive) ITG promoted greater downstream tau spreading. We then compared these subgroups using a Mann-Whitney U test. The number of downstream regions assessed in these analyses was first set to 30, but we also addressed effects over a range of this parameter from 20 to 50 (see [Table S6](#)).

Network model-based subject stratification

Our findings suggested two important transitions during the natural history of AD, based on: (1) remote A β -tau interaction within the lateral EC and (2) local A β -tau interaction within the ITG. To examine subjects’ status with respect to these transitions, we computed quantitative thresholds for each metric. The first threshold was computed by multiplying the regional cutoff of the EC remote A β influence metric by the tau W-score cutoff (2.5 in our study). Similarly, for the second threshold, the regional cutoff for the ITG local amyloid SUVR was multiplied by the tau W-score cutoff. Using this approach, we classified each subject into one of four groups: (1) least affected by the tau pathology (“tau-negative”) in EC ([Baek et al., 2020](#)), (2) subthreshold EC remote A β -tau interaction despite the presence of EC tau (“latent tau” group), (3) suprathreshold EC remote A β -tau interaction but subthreshold ITG A β -tau local interaction (“spreading tau” group), and (4) suprathreshold ITG A β -tau local interaction (“propagating tau” group). Values for each metric were calculated in each hemisphere separately. Subjects were assigned to the latent tau group if they had subthreshold values in both hemispheres for Threshold 1, whereas they were stratified to the propagating tau group if they had suprathreshold values in both hemispheres for Threshold 2. If one hemisphere would yield assignment to the latent tau and the other to propagating tau group, then the subject was assigned to the latent tau group, based on the notion that they might, upon re-testing, move into the spreading tau group as defined.